Electronic/mass transport increased hollow porous Cu₃P/MoP nanospheres with strong electronic interaction for promoting oxygen reduction in Zn-air batteries

Man Guo [a], Meijiao Xu [a], Yuan Qu [a], Chuan Hu [a], Puxuan Yan [a], Tayirjan Taylor Isimjan [b,*], Xiulin Yang [a,*]

[a] Guangxi Key Laboratory of Low Carbon Energy Materials, School of Chemistry and Pharmaceutical Sciences, Guangxi Normal University, Guilin, 541004, China
[b] Saudi Arabia Basic Industries Corporation (SABIC) at King Abdullah University of Science and Technology (KAUST), Thuwal, 23955-6900, Saudi Arabia

ARTICLE INFO

ABSTRACT

Developing high-efficient non-noble metal-based catalysts for oxygen reduction reaction (ORR) is an inevitable way to improve Zinc-air batteries' performance (ZAB). Herein, we report a Cu₃P/MoP electrocatalyst (Cu₃P/MoP@C) supported by hollow-porous-carbon nanospheres displaying high electrocatalytic activity and exceptional durability in alkaline media. The optimized ORR catalyst outperformed the benchmark Pt/C (20 wt%) and most recently reported Cu-/Mo-based catalysts in various aspects. X-ray photoelectron spectroscopy reveals that the excellent ORR performance originates from the charge transfer between of Cu₃P and MoP species. Besides, the large specific surface area of Cu₃P/MoP@C with mesoporous structure is particularly advantageous for the inner surface contact with electrolyte to accelerate ORR kinetics. Moreover, Cu₃P/MoP@C also exhibits a large power density of 156 mW cm⁻², a high round-trip efficiency, and superb stability over 231 h superior to Pt/C in the ZAB. This work offers a scalable and promising approach for the rational fabrication of hollow porous structure materials.

1. Introduction

Growing energy demands and environmental deterioration issues have compelled the pursuit of renewable energy conversion-storage technologies, for instance, fuel cells and metal-air batteries [1–3]. Especially, Zinc-air batteries (ZAB) have obtained considerable attention due to their high theoretical energy density of 1086 Wh kg⁻¹, good safety and environmental benignity [4–6]. However, practical and large-scale commercial implementation of ZAB is lagged owing to their performance is severely affected by the sluggish kinetics of ORR [7,8]. Although Pt-based catalysts are the state-of-the-art ORR electrocatalyst to date, there is high cost, natural scarcity, poor stability, and vulnerability to methanol poisoning greatly restrict their widespread applications [9–11]. As a result, it is imperative to develop cost-effective, high-efficient and earth-abundant alternative Pt-based catalysts to living up to the high-performance requirement of ZAB and promote ORR activity.

In recent years, transition metal phosphides (TMPs) and their compounds are emerging as a promising alternative to Pt-based catalysts due

to their natural abundance and cost-efficient. Importantly, previous reports have demonstrated that their ORR properties can be enhanced significantly through rational design [12–15]. However, as compared to other cathodic electrocatalysts, The ZAB of based TMPs is rarely reported because of the low specific surface area, insufficient electrical conductivity, and aggregation [16], but when TMPs such as Cu₃P is combined simultaneously with other carbon based substrates to form a composite material, the carbon component in the material improves conductivity; also, the synergy between various components enhances the ORR activity [17,18]. In catalytic processes, there is a consensus that electrocatalytic activity can be improved significantly by exposing more active sites [19]. In this regard, it is necessary to design and synthesize high surface area electrocatalysts with a high porosity conducive to mass transport and increase the availability of active sites, which are pivotal for enhancing the electrocatalytic performance of ORR.

In this work, we reported a rational design of the hollow porous spherical structure of Cu₃P/MoP@C by high-temperature phosphating using carbon spheres as support under argon flow. The optimized catalyst exhibits excellent ORR catalytic activity under alkaline

---
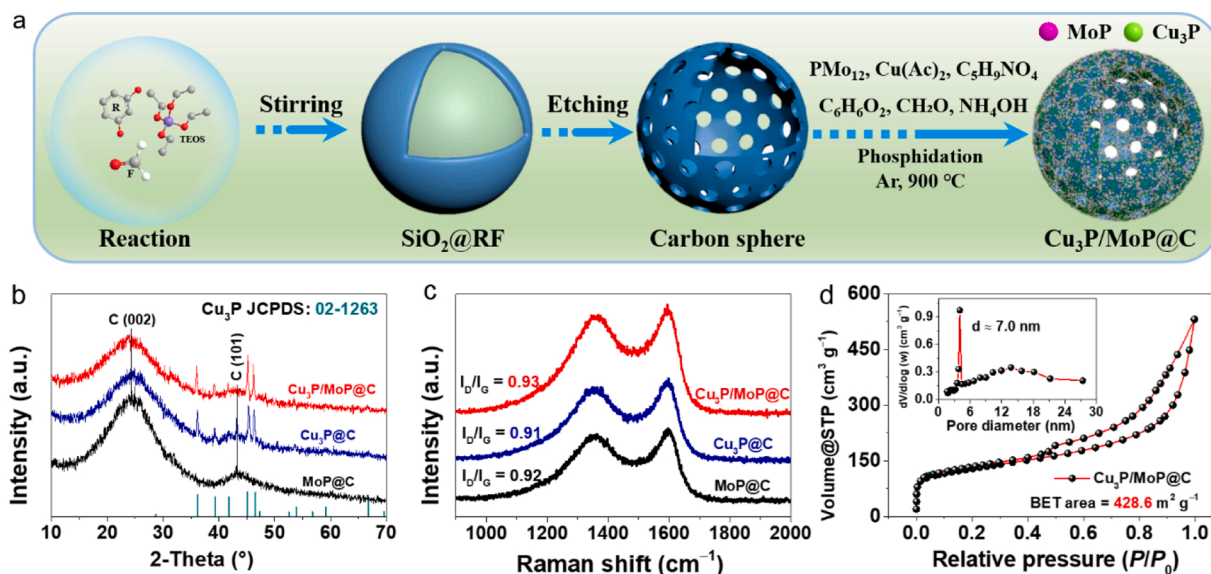
Fig. 1. (a) Schematic illustration of preparation $Cu_3P/MoP@C$. (b) XRD patterns and (c) Raman spectra of $Cu_3P/MoP@C$, $Cu_3P@C$, $MoP@C$. (d) N_2 adsorption-desorption isotherm with the inset showing the corresponding pore size distribution of $Cu_3P/MoP@C$.

conditions with a half-wave potential ($E_{1/2}$) of 0.90 V (vs. RHE) superior to commercial Pt/C (0.84 V vs. RHE) and a majority of Cu-/Mo-based ORR electrocatalysts (the RHE calibration was shown in Fig. S1). Furthermore, $Cu_3P/MoP@C$ also demonstrates outstanding long-term stability compared to Pt/C with a slight current attenuation of 2% after 40000 s tests. The detailed characterizations indicate that the superior activity is attributed to a strong interaction between Cu_3P and MoP species, high BET specific surface area, and porous structure facilitated mass transport. More importantly, the ZAB based on $Cu_3P/MoP@C$ achieves a high open-circuit voltage (OCV) of 1.51 V, a peak power density of 156 mW cm^{-2}, and the $Cu_3P/MoP@C$ + RuO_2 based ZAB has little decay after 231 h durability testing at a current density of 5 mA cm^{-2}, certifying its promising application in advanced energy conversion-storage devices.

2. Experimental section

2.1. Chemicals and reagents

Ethanol, formaldehyde solution (CH_2O), tetraethyl silicate (TEOS), resorcinol ($C_6H_6O_2$), 1,3,5-benzenetricarboxylic acid (BTC), and zinc acetate dihydrate ($Zn(Ac)_2$) were purchased from Xilong Chemical Co., Ltd. Phosphomolybdic acid hydrate (PMo_{12}), copper (II) acetate monohydrate ($Cu(Ac)_2 \cdot H_2O$), and L-glutamic acid ($C_5H_9NO_4$) were bought from Sinopharm Chemical Reagent Co., Ltd. (Shanghai China). Ammonia solution (NH_4OH), potassium hydroxide and red phosphorus (P) were got from Aladdin Industrial Corporation. Nafion solution (5 wt %) and platinum on carbon (Pt/C, 20 wt%) were obtained from Alfa Aesar and Macklin Biochemical, respectively. All chemicals and reagents were of analytical grade and used directly without further purification.

2.2. Synthesis of carbon spheres

Hollow mesoporous carbon spheres were obtained according to the previously reported work with slightly modification [20]. In the protocol, 3.46 mL of TEOS was quickly added to a stirred mixture of deionized water (10 mL), ethanol (70 mL) and NH_4OH (3 mL). After 15 min, 3.63 mmol $C_6H_6O_2$ and 0.56 mL of CH_2O were added to the above mixture. The mixture was stirred vigorously at room temperature for 24 h, and centrifuged at 9000 rpm for 6 min to obtain $SiO_2@RF$ nanospheres (R and F represent resorcinol and formaldehyde solution, respectively,

which is a process of coating a layer of carbonaceous material on the surface of SiO_2 by an aldol condensation reaction). The nanospheres were washed with ethanol for several times and dried overnight in an oven at 60 °C.

The $SiO_2@RF$ was placed in a clean quartz boat and transferred to a tube furnace for heating at 700 °C in a nitrogen atmosphere for 5 h with a heating rate of 5 °C min^{-1} to obtain $SiO_2@C$. Carbon spheres were obtained by removing SiO_2 core with 3 M KOH at 60 °C.

2.3. Synthesis of $Cu_3P/MoP@C$

In a synthetic procedure, a certain amount of carbon spheres were dispersed in 50 mL of deionized water containing 0.02 mmol PMo_{12}, 0.1 mmol $Cu(Ac)_2 \cdot H_2O$ and 0.03 mmol $C_5H_9NO_4$ and ultrasonicated for 30 min so that carbon spheres can be uniformly dispersed in the solution. After that, 50 mL of ethanol solution containing 0.1 mmol BTC was quickly added to the above solution. After vigorous stirring for 6 h, 1.82 mmol $C_6H_6O_2$, 0.28 mL of CH_2O and 2 mL of NH_4OH were sequentially added the above mixture. After continuous stirring for 24 h under ambient conditions, the precursors were separated by centrifugation, washed with ethanol for 3 times, and dried overnight at 60 °C. 50 mg of precursor powder was ground together with 100 mg of red phosphorus, transferred to a porcelain boat, and calcined at different temperatures (800, 900, 1000 °C) for 2 h under Ar flow with a 5 °C min^{-1} heating rate. Unless specifically stated, the $Cu_3P/MoP@C$ was obtained at 900 °C.

For comparison, the Cu doping level was first tuned by altering the Cu/Mo molar ratio (10:1, 1:1, 1:5, 1:10) during the synthesis process. Second, the mass ratio of precursor and red phosphorus was changed (1:1, 1:3, 2:1, 3:1) during the calcination process.

2.4. Synthesis of $Cu_3P@C$ and $MoP@C$

The $Cu_3P@C$ and $MoP@C$ were synthesized using a similar method as $Cu_3P/MoP@C$ mentioned above, except that only PMo_{12} or $Cu(Ac)_2 \cdot H_2O$ are added during the synthesis.

2.5. Zn-air batteries (ZAB) fabrication and test

The catalyst slurry was prepared by ultrasonically dispersing 2 mg of catalyst and 5 μL of 5 wt % Nafion into a mixed solution of 150 μL of water and 50 μL of isopropanol, coating the obtained slurry on hydro-
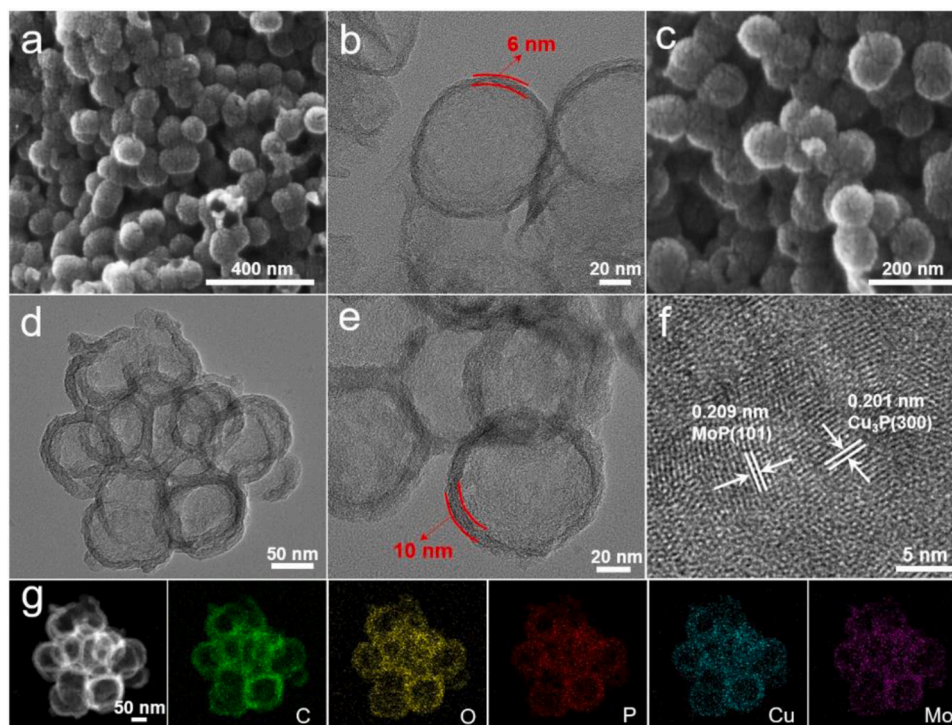
Fig. 2. (a) SEM and (b) TEM images of carbon spheres. (c) SEM, (d, e) TEM, (f) HR-TEM, and (g) HAADF-STEM images and the corresponding elemental mappings of Cu$_3$P/MoP@C.

philic carbon paper (loading:1 mg cm^{-2}) and dried at room temperature to be used as the air cathode. Zinc foil was employed as the anode, and the 6.0 M KOH solution containing 0.2 M Zn(Ac)$_2$ was served as the electrolyte to assemble the Zinc-Air battery. Since Cu$_3$P/MoP@C showed a poor OER performance (Fig. S2), a Cu$_3$P/MoP@C + RuO$_2$ (mass ratio = 1:1) was used as an air cathode during the stability test by applying the same preparation method as above. For comparison, Pt/C + RuO$_2$ was also tested under the same conditions. The polarization curve and the open circuit voltage (OCV) were obtained by using electrochemical workstation (CHI 760E) under ambient conditions, and the stability of the ZAB was tested by using the LAND battery testing system (BT2016A) at a current density of 5 mA cm^{-2} for 20 min at each charge-discharge cycle. For comparison, the 20 wt% Pt/C based ZAB was also studied under the same conditions. The specific capacity was calculated according to the following equation [21]:

$$Specific\ capacity = \frac{discharge\ current \times time}{weight\ of\ consumed\ Zinc}$$

3. Results and discussion

3.1. Synthesis and structural analysis of catalysts

The Cu$_3$P/MoP@C composite was obtained by impregnation and high-temperature phosphating methods to load the hybrid Cu$_3$P/MoP on hollow porous carbon spheres, as shown in Fig. 1a. Briefly, carbon spheres were ultrasonically dispersed in a mixed aqueous Cu(Ac)$_2$·H$_2$O, PMo$_{12}$, and C$_5$H$_9$NO$_4$, then the ethanol solution of BTC was added dropwise into the above solution under vigorous stirring. Finally, C$_6$H$_6$O$_2$, CH$_2$O, and NH$_4$OH were added in sequence after 6 h. The ammonia solution acted as a catalyst for aldol condensation reaction, coating a layer of carbon on the composite's surface (details in the experimental section). During the calcination, red phosphorus (P) is used as a phosphorus source does not generate toxic PH$_3$ gas at high temperature compared with NaH$_2$PO$_2$ approach.

The crystalline characteristics of the as-prepared catalysts were elucidated by X-ray diffraction (XRD) patterns (Fig. 1b). In addition to the broad peaks at around 24.8° and 43.3° belonging to (002) and (101) facets of graphitic carbon [22,23], and diffraction peaks at around 36.2°, 39.3°, 41.7°, 45.1°, and 46.3° can be assigned to the (112), (202), (211), (300) and (113) lattice planes of hexagonal Cu$_3$P (JCPDS: 02–1263), respectively [17,24]. Because the diffraction peaks of MoP are not prominent, it is likely to have a low crystallinity. The content of Mo loading onto the Cu$_3$P/MoP@C is up to 12.85 wt% measured by inductively coupled plasma mass spectroscopy (ICP-MS) (Table S1). The above results demonstrate Cu$_3$P/MoP has been successfully fabricated on the carbon matrix. Furthermore, the intensity ratio of the D band and G band (I$_D$/I$_G$), an evaluation index of carbon disorders, were given in the Raman spectra (Fig. 1c). The I$_D$/I$_G$ of Cu$_3$P/MoP@C was 0.93, which is roughly consistent with Cu$_3$P@C (0.91) and MoP@C (0.92), indicating that the surface disorder caused by loading metal is approximately the same [25,26]. Raman spectroscopy was shown in Fig. S3. The graphitization degree can be adjusted by changing the calcination temperature and copper and phosphorus contents during the synthesis process. The N$_2$ adsorption-desorption isotherm was illustrated in Fig. 1d, which presented reversible type IV isotherm with a remarkable hysteresis loop have confirmed the presence of mesoporous [22,27]. The Brunauer–Emmett–Teller (BET) specific surface area and average pore size of Cu$_3$P/MoP@C were calculated to be 428.6 m^2 g^{-1} and ~7 nm, which were important factors to improve electrocatalytic activity due to increase the maximum utilization of active sites and promote mass transport [28].

The morphology of samples was characterized by scanning electron microscopy (SEM) and transmission electron microscopy (TEM). The surface of SiO$_2$@RF nanospheres was smooth, whereas the surface of hollow nanospheres obtained after removing the SiO$_2$ core was rough and cracked (Figs. 2a-b and S4a–c), demonstrating the formation of pores, which was in good accordance with BET test results and its shell was approximately 6 nm thick. The porous carbon sphere maintained complete after Cu$_3$P/MoP was supported on carbon spheres, except that the shell was increased to 10 nm thick (Figs. 2c–e and S5). The lattice fringes of Cu$_3$P/MoP@C were observed from high-resolution TEM (HR-

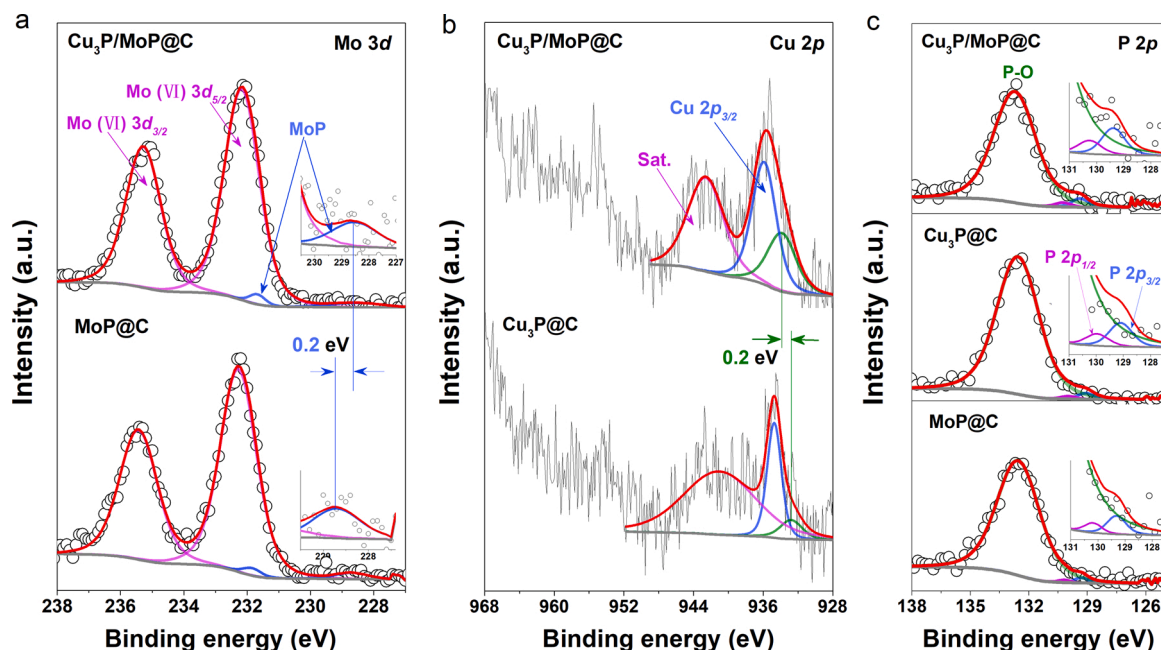**Fig. 3.** High-resolution XPS spectra of (a) Mo 3*d*, (b) Cu 2*p*, and (c) P 2*p* regions in Cu₃P/MoP@C, Cu₃P@C, MoP@C, respectively.

TEM) images, of which 0.209 nm and 0.201 nm were consistent with the (101) crystal plane of MoP and the (300) crystal plane of Cu₃P, respectively (Fig. 2f) [29]. As shown in Figs. 2g and S6, the hollow porous structure was further reaffirmed by high-angle annular dark-field scanning transmission electron microscopy (HAADF-STEM), as well the corresponding energy-dispersive X-ray spectroscopy (EDS) mappings confirmed the uniform dispersion of C, O, P, Cu, and Mo on the Cu₃P/MoP@C structure. The results obtained further supported XRD analysis to evidence the successful formation of Cu₃P/MoP on the carbon spheres.

XPS spectra probed the chemical states and composition of elements. The survey XPS spectra (Fig. S7) show that Mo, Cu, C, P, and O elements are dominant in the catalysts. For Cu₃P/MoP@C, the high-resolution C

1*s* spectrum is deconvoluted into four peaks at =284.8(C—C), 286.1 (C—O) and 289.1 eV (C=O) (Fig. S8) [30,31]. The Mo 3*d* XPS spectrum of Cu₃P/MoP@C shows peaks at around 228.5 and 231.7 eV are indexed to Mo$^{\delta+}$ species ($0 < \delta < 4$) in MoP [32–34]. The other two peaks located at 232.2 eV and 235.3 eV coincide with Mo (Ⅵ) $3d_{3/2}$ and $3d_{5/2}$ of MoO₃, respectively, which might arise from the surface oxidation of MoP. Compared with MoP@C, the binding energies of Mo-P are negatively shifted by 0.2 eV (Fig. 3a). Moreover, the Cu 2*p* XPS spectrum of Cu₃P/MoP@C was fitted into three peaks assigned to Cu-P (933.1 eV), Cu-O (935.2 eV) and one satellite peak (942.1 eV) [17,35], respectively, the presence of Cu-O bond is unavoidable due to the surface oxidation of Cu₃P. Contrary to Mo 3*d*, the binding energies of Cu-P are positively shifted at 0.2 eV than Cu₃P@C (Fig. 3b). Meanwhile, the P 2*p* region of
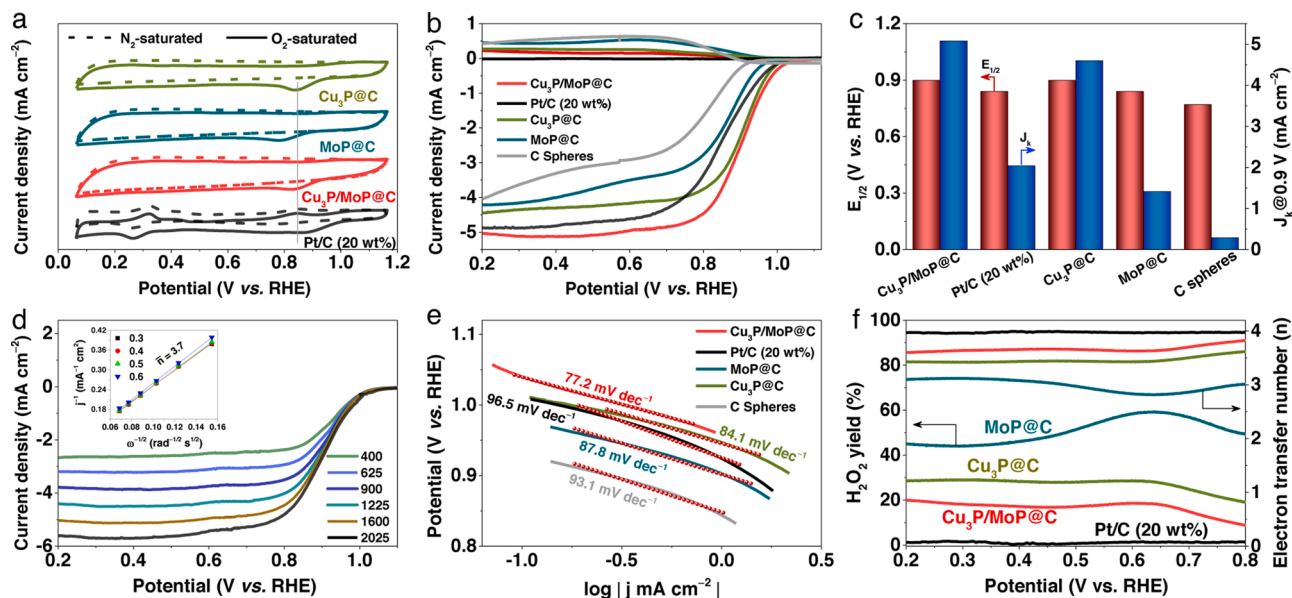
Fig. 4. Electrochemical performance of different catalysts. (a) CV curves in N₂ or O₂-saturated 0.1 M KOH solutions. (b) LSV polarization curves in O₂-purged 0.1 M KOH electrolyte and (c) the corresponding half-wave potential ($E_{1/2}$) and kinetic current density (J_k) at 0.9 V. (d) Polarization curves of Cu₃P/MoP@C with various rotating speeds from 400 to 2025 rpm and the corresponding K-L plots (inset). (e) Tafel plots and (f) H₂O₂ yield (%) and electron transfer number (*n*) from various catalysts.

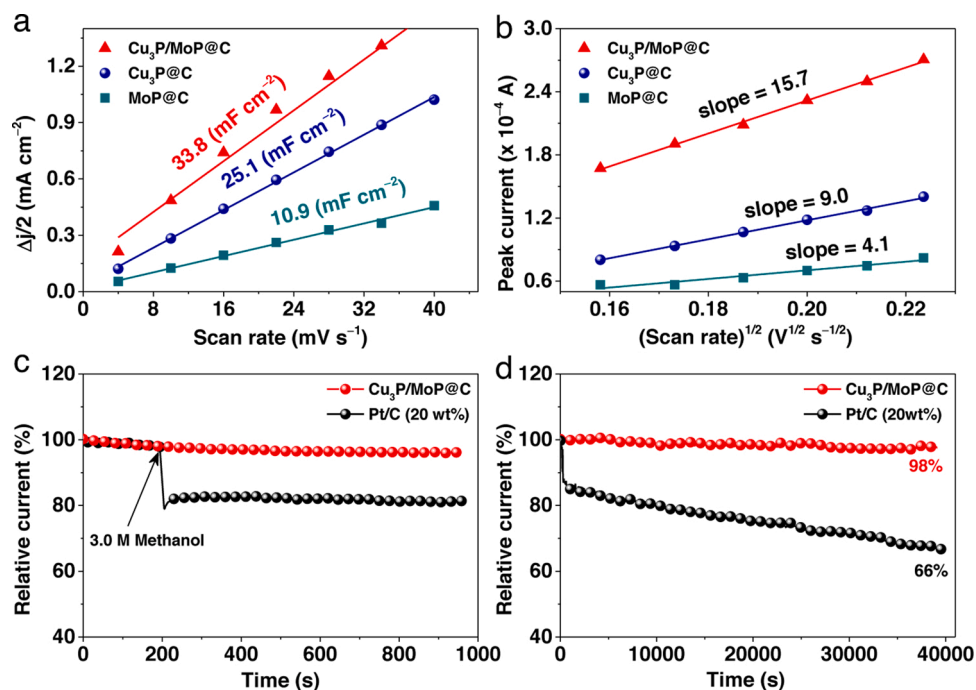**Fig. 5.** (a) The double-layer capacitance (C_{dl}) values of Cu₃P/MoP@C, Cu₃P@C, and MoP@C. (b) CV fitting curves in 0.1 M KCl containing 5 mM K₃[Fe(CN)₆] solution at various scan rates. (c) Methanol tolerance tests of Cu₃P/MoP@C and Pt/C (20 wt%) in 0.1 M KOH with the addition of 3 M methanol at around 200 s and (d) the corresponding stability test in O₂-saturated 0.1 M KOH solution at a rotating speed of 1600 rpm.

Cu₃P/MoP@C is deconvoluted into three peaks at 129.4, 130.3, and 133.7 eV (Fig. 3c), and ascribed to $2p_{3/2}$ and $2p_{1/2}$ of Mo—P or Cu—P, and P—O bonds due to surface oxidation caused by phosphorus [17,32,36]. The C–P bonds was not found in the C 1s and P 2p spectra indicating no P-doping on the carbon frame (Figs. 3c and S7) [37]. It is worth noting that the positive shift on Cu-P and the negative shift on Mo-P binding energies in Cu₃P/MoP@C evidence the charge transfer from the Cu₃P to the MoP, interpreting the strong electronic interaction between Cu₃P and MoP species [33,38]. Moreover, the high-resolution N 1s spectrum shows a small amount of nitrogen that exists in the form of pyridinic N (398.0 eV) and pyrrolic N (400.6 eV) (Fig. S9) [39], indicating N-doping in the carbon frame result of the ammonia treatment during the synthesis. However, the contribution of the N-doping to ORR performance is not discussed separately since it is the common step for all the catalysts. Overall, as expected, XPS analysis further confirmed that the Cu₃P/MoP was successfully synthesized on the carbon spheres, which is consistent with TEM and XRD analysis.

3.2. ORR activities of electrocatalysts in alkaline medium

The ORR performance was measured by rotating disk electrode (RDE) and rotating ring disk electrodes (RRDE) techniques in 0.1 M KOH solution. The optimized calcination temperature and the doping content, and the corresponding performance parameters are shown in Figs. S10–12. The ORR polarization curves of all samples were recorded in O₂-saturated 0.1 M KOH. The resulting onset potential (E_{onset}) and half-wave potential ($E_{1/2}$) are listed in Table S2. In general, the higher the onset potential shows better electrocatalytic activity in the LSV polarization curve [40,41]. The results showed that the best catalyst, designated as Cu₃P/MoP@C, was obtained when the molar ratio of Cu/Mo was 5/1, the mass ratio of P with precursor was 2/1 together with an annealing temperature was 900 °C. Therefore, if not explicitly stated, the optimized catalyst here is the target catalyst discussed below.

Cyclic voltammetry (CV) curves were recorded in O₂/N₂-saturated 0.1 M KOH solution. As displayed in Fig. 4a, the distinct cathodic peaks were observed in all samples under O₂-saturated electrolyte compared to

N₂-saturated solution, indicating an efficient ORR process. The linear sweep voltammetry (LSV) curves were tests in O₂-saturated 0.1 M KOH are presented in Fig. 4b, the Cu₃P/MoP@C exhibits an incremental E_{onset} (1.03 V) and $E_{1/2}$ (0.90 V) in contrast to those of carbon spheres (0.94 V, 0.77 V) and Cu₃P@C (1.02 V, 0.90 V), MoP@C (1.00 V, 84 V) and commercial Pt/C (1.02 V, 0.84 V). Meanwhile, the kinetic current density (J_k) of Cu₃P/MoP@C reaches 5.08 mA cm⁻² at 0.9 V, which outperforms those of carbon spheres (0.29 mA cm⁻²), Cu₃P@C (4.60 mA cm⁻²), MoP@C (1.41 mA cm⁻²) and commercial Pt/C (2.04 mA cm⁻²) (Fig. 4c). The LSV curves are obtained at the same rotational speed (1600 rpm) to minimize the effect of the mass transfer process. Nevertheless, the current density of Cu₃P/MoP@C (5.13 mA cm⁻²) is 19 % and 28 % higher than those of Cu₃P@C (4.30 mA cm⁻²) and MoP@C (4.00 mA cm⁻²) at 0.4 V (vs. RHE). Moreover, the number is 19 % and 42 % higher at 0.6 V (vs. RHE), respectively, which is much more pronounceable than the similar studies reported in the literature under the same voltages suggesting the synergy between the Cu₃P and MoP species resulted by the charge transfer [42,43]. All the data suggested that the Cu₃P/MoP@C catalyst possesses the highest ORR electrocatalytic activity and Cu₃P@C is the main activity center. The outstanding ORR performance of Cu₃P/MoP@C is ascribed to the strong synergistic interaction between Cu₃P and MoP. Besides, LSV curves were also obtained at varying rotational speeds from 400 to 2025 rpm (Fig. 4d), and the resulted Koutechy-Levich (K-L) plots possess an excellent linear relationship (inset), which reveals first-order reaction kinetics related to the concentration of dissolved oxygen [44]. The average number of electron transfer number (n) is estimated to be ~3.7 based on the K-L plots at various potentials, corroborating that oxygen can be reduced through the direct four-electron pathway. To demonstrate that the rapid ORR kinetics of the as-prepared catalysts, Fig. 4e illustrates the corresponding Tafel slopes of Cu₃P/MoP@C, carbon spheres, Cu₃P@C, MoP@C, and commercial Pt/C are calculated to be 77.2, 93.1, 84.1, 87.8, and 96.5 mV dec⁻¹, respectively. Simultaneously, the electrochemical impedance spectroscopy (EIS) was tested shown in Fig. S13; the Cu₃P/MoP@C shows a smaller charge transfer resistance (R_{ct}, 66 Ω) than other catalysts, which further proves that the high charge transport
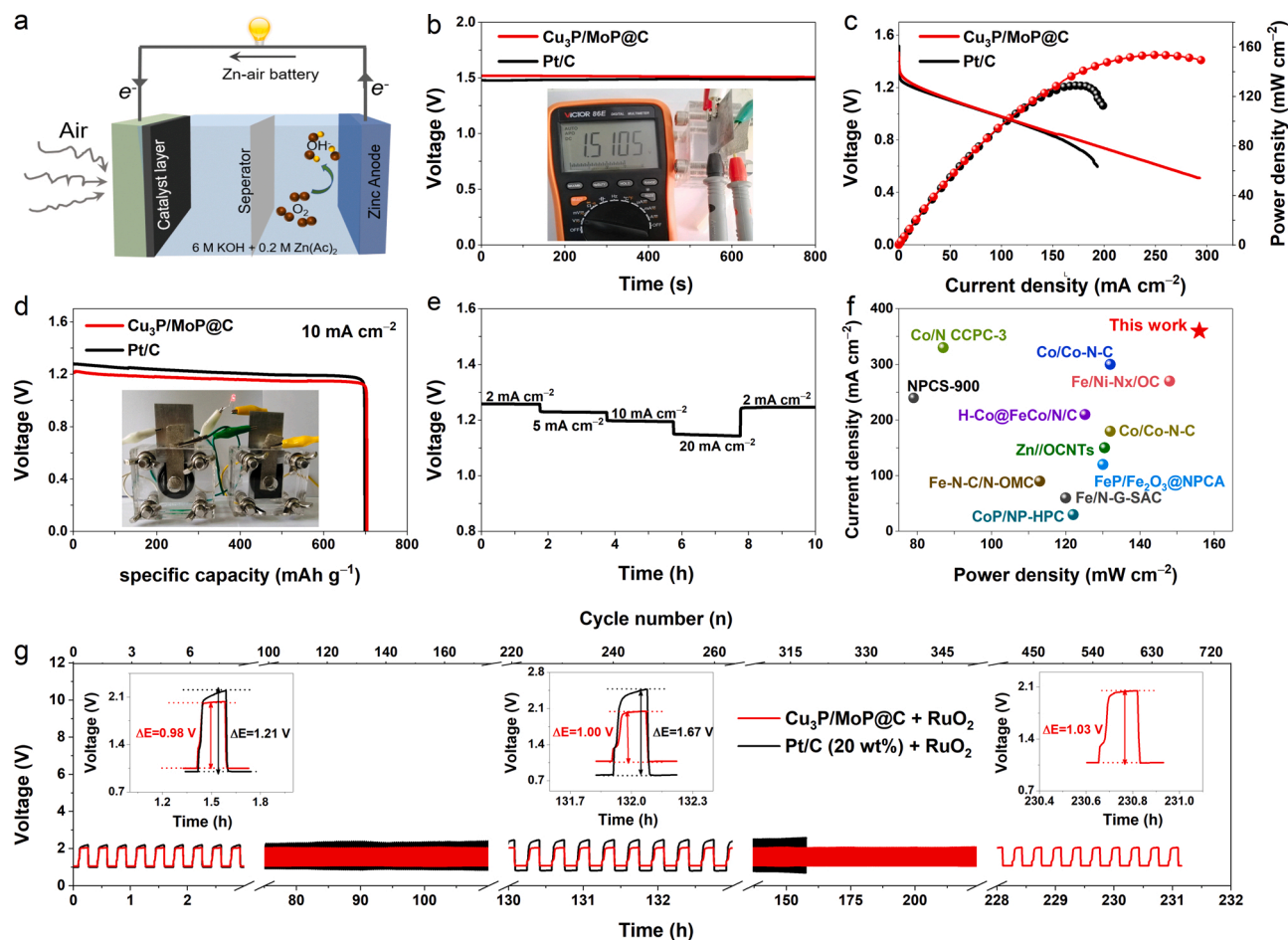
Fig. 6. Performance of self-assembled Zinc-air batteries (ZAB) with $Cu_3P/MoP@C$ and Pt/C (20 wt%) as air cathode. (a) Schematic configuration of assembled ZAB. (b) Open-circuit voltage (OCV) plots (inset: photography of OCV of the ZAB tested with a multimeter). (c) Discharge polarization curves and the corresponding power densities of the catalysts. (d) Specific capacity plots (inset: photograph of the LED lit up by two Zn-air batteries in series). (e) Discharge profiles at various current densities. (f) Comparison of $Cu_3P/MoP@C$ as air cathode with other recently reported excellent catalysts, in terms of power and current density. (g) Galvanostatic cycling at 5 mA cm^{-2} (20 min for each cycle).

kinetics of $Cu_3P/MoP@C$ [45,46]. To further interrogate the mechanism of $Cu_3P/MoP@C$ promote ORR activity, the RRDE technique was executed to verify n close to 4, consistent with the value based on the K-L plots. The calculated H_2O_2 yield is 20 % or less on the potential range of 0.2−0.8 V vs. RHE, implying that the reduced product exhibits superior selectivity (Fig. 4f). These excellent performances reveal that the ORR activity of $Cu_3P/MoP@C$ catalyst not just surpasses commercial Pt/C but compares favorably with the majority of recently reported advanced Cu-/Mo-based ORR electrocatalysts (Table S3).

The electrochemical active surface area (ECSA) was evaluated by the double-layer capacitance (C_{dl}) to explain the intrinsic ORR activity further. The ECSA has a positive correlation with C_{dl}, and C_{dl} is calculated according to the CV curve in the non-faradic region at different scan rates (Fig. S14) [47–49]. As shown in Fig. 5a, the $Cu_3P/MoP@C$ presents a C_{dl} value of 33.8 m F cm^{-2}, being beyond that of $Cu_3P@C$ (25.1 m F cm^{-2}) and $MoP@C$ (10.9 m F cm^{-2}), indicating $Cu_3P/MoP@C$ has a higher ECSA, which can expose more active sites and promote ORR activity. Subsequently, ECSA was further reaffirmed by testing CV at different sweep speeds in the mixed solution of 0.5 mM $K_3[Fe(CN)_6]$ and 0.1 M KCl (Fig. S15). A pair of prominent redox peaks were observed in all samples' CV curves, and the corresponding CV fitting curves are shown in Fig. 5b, which are consistent with C_{dl} trends, indicating $Cu_3P/MoP@C$ has a higher ECSA compared with other catalysts [39]. The chronoamperometric response was measured in O_2-saturated 0.1 M KOH at a rotation rate of 1600 rpm to assess stability and methanol

tolerance. As depicted in Fig. 5c and d, the $Cu_3P/MoP@C$ seemed to be immune and maintain a constant current density after 3 M methanol was rapidly injected into electrolyte at 200 s, whereas the Pt/C current density drops sharply. Furthermore, the current density of $Cu_3P/-MoP@C$ retained 98 % of its initial value after approximately 40000 s, which was significantly higher than the commercial Pt/C (66 %). The results indicated that $Cu_3P/MoP@C$ was endowed with good durability and a subtle methanol crossover effect, attributing to the porous carbon skeleton structure and the strong synergistic effect Cu_3P and MoP species [50]. These properties are critical to the practical application of $Cu_3P/MoP@C$ electrocatalyst.

3.3. Test for performance of assembled Zinc-air batteries (ZAB)

Considering the outstanding ORR performance of $Cu_3P/MoP@C$, we assembled a ZAB to evaluate the application potential of $Cu_3P/MoP@C$ in real energy conversion equipment. Pt/C is also tested under the same conditions as the benchmark. The schematic diagram of ZAB is presented in Fig. 6a. The open-circuit voltage (OCV) of ZAB is 1.51 V, slightly larger than Pt/C (1.48 V) (Fig. 6b). Additionally, the maximum power density of $Cu_3P/MoP@C$ is 156 mW cm^{-2} at 245 mA cm^{-2}, greatly exceeding commercial Pt/C (131 mW cm^{-2} at 170 mA cm^{-2}) and others recently reported catalysts (Fig. 6c, f), which implied that $Cu_3P/MoP@C$ has better performance. The specific-capacity was calculated based on the normalized mass of consumed Zinc. As shown in Fig. 6d,

the ZAB of based $Cu_3P/MoP@C$ yield slight higher specific capacity (704 mAh g_{Zn}^{-1}, ~87.8 % utilization of the theoretical capacity of 820 mAh g_{Zn}^{-1}) relative to commercial Pt/C (699 mAh g_{Zn}^{-1}, 85.2 % utilization of the theoretical capacity of 820 mAh g_{Zn}^{-1}) [51]. The two ZAB connected in-series can provide enough voltage to illuminate a LED (~3.0 V) (inset). Subsequently, Fig. 6e presents discharge curves at different current densities, when the current density returned to 2 mA cm^{-2} with only a voltage loss rate of 0.8 %, indicating that the $Cu_3P/MoP@C$ possesses excellent rate performance [52]. Galvanostatic cycling tests showed that the $Cu_3P/MoP@C$ + RuO_2-based ZAB could continuously keep working for over 231 h, and the voltage gap (ΔE) between charge and discharge is negligible. By contrast, the ZAB of based Pt/C + RuO_2 is capable of operating steadily for only ~157 h with a significant ΔE (Fig. 6g), suggesting the former had a higher round-trip efficiency. Taken together, it demonstrated that $Cu_3P/MoP@C$ has excellent ORR activity and has the potential for practical application in Zn-air batteries.

Based on the above experimental results, the $Cu_3P/MoP@C$ shows outstanding ORR activity and stability compared to $Cu_3P@C$ and MoP@C, indicating that the strong electronic interaction of Cu_3P and MoP species reduce the charge transfer impedance and enhance ORR kinetics, which has been affirmed by XPS analysis and EIS results [53]. Apart from that, the hollow mesoporous $Cu_3P/MoP@C$ with a large specific surface area, which is beneficial to expose more active sites and provide high contact area with electrolytes to expedite electron and mass transport efficiently [54–56]. These excellent properties endow the $Cu_3P/MoP@C$ one of the most promising ORR electrocatalysts.

4. Conclusions

To summarize, we have innovatively adopted carbon spheres as a template, combined with impregnation and high-temperature pyrolysis to co-anchor Cu_3P and MoP on a hollow porous carbon support. The resulting $Cu_3P/MoP@C$ exhibit outstanding ORR activity in alkaline solution compared with monometallic phosphide. XPS and BET analysis showed that high ORR activity is due to the strong synergistic effect between Cu_3P and MoP and the porous structure with a large specific surface area. The aqueous ZAB was assembled with $Cu_3P/MoP@C$ as an air cathode due to its remarkable electrocatalytic performance. The ZAB achieved a high power density of 156 mW cm^{-2}, a specific capacity of 704 mAh g_{Zn}^{-1}, and a high round-trip efficiency demonstrated by the lower charge-discharge voltage gap and robust stability for over 231 h superior to the ZAB based on Pt/C + RuO_2 and most currently reported advanced electrocatalysts. Our synthetic strategy of preparing bimetallic phosphide can be extended to the design and synthesis of other hollow porous electrocatalysts for sustainable energy conversion and storage devices.

CRediT authorship contribution statement

Man Guo: Writing - original draft. **Meijiao Xu:** Investigation, Methodology. **Yuan Qu:** Data curation, Conceptualization. **Chuan Hu:** Investigation. **Puxuan Yan:** Data curation, Methodology. **Tayirjan Taylor Isimjan:** Writing - review & editing. **Xiulin Yang:** Supervision, Writing - review & editing.

Declaration of Competing Interest

The authors report no declarations of interest.

Acknowledgements

Appendix A. Supplementary data

Supplementary material related to this article can be found, in the online version, at doi:https://doi.org/10.1016/j.apcatb.2021.120415.

References

[1] P. Prabhu, V. Jose, J.-M. Lee, Design strategies for development of TMD-based heterostructures in electrochemical energy systems, Matter 2 (2020) 526–553.

[2] V. Jose, J.M.V. Nsanzimana, H. Hu, J. Choi, X. Wang, J.-M. Lee, Highly efficient oxygen reduction reaction activity of N-doped carbon–cobalt boride heterointerfaces, Adv. Energy Mater. 11 (2021), 2100157.

[3] H. Wang, J. Li, K. Li, Y. Lin, J. Chen, L. Gao, V. Nicolosi, X. Xiao, J.-M. Lee, Transition metal nitrides for electrochemical energy applications, Chem. Soc. Rev. 50 (2021) 1354–1390.

[4] X. Hu, Y. Chen, M. Zhang, G. Fu, D. Sun, J.-M. Lee, Y. Tang, Alveolate porous carbon aerogels supported Co_9S_8 derived from a novel hybrid hydrogel for bifunctional oxygen electrocatalysis, Carbon 144 (2019) 557–566.

[5] G. Fu, X. Yan, Y. Chen, L. Xu, D. Sun, J.-M. Lee, Y. Tang, Boosting bifunctional oxygen electrocatalysis with 3D graphene aerogel-supported Ni/MnO particles, Adv. Mater. 30 (2018), 1704609.

[6] G. Fu, Y. Wang, Y. Tang, K. Zhou, J.B. Goodenough, J.-M. Lee, Superior oxygen electrocatalysis on nickel indium thiospinels for rechargeable Zn–air batteries, ACS Mater. Lett. 1 (2019) 123–131.

[7] M. Luo, W. Sun, B.B. Xu, H. Pan, Y. Jiang, Interface engineering of air electrocatalysts for rechargeable zinc–air batteries, Adv. Energy Mater. 11 (2020), 2002762.

[8] J. Liu, J. Bak, J. Roh, K.-S. Lee, A. Cho, J.W. Han, E. Cho, Reconstructing the coordination environment of platinum single-atom active sites for boosting oxygen reduction reaction, ACS Catal. 11 (2021) 466–475.

[9] G. Fu, J. Wang, Y. Chen, Y. Liu, Y. Tang, J.B. Goodenough, J.-M. Lee, Exploring indium-based ternary thiospinel as conceivable high-potential air-cathode for rechargeable Zn–air batteries, Adv. Energy Mater. 8 (2018), 1802263.

[10] G. Fu, X. Jiang, Y. Chen, L. Xu, D. Sun, J.-M. Lee, Y. Tang, Robust bifunctional oxygen electrocatalyst with a "rigid and flexible" structure for air-cathodes, NPG Asia Mater. 10 (2018) 618–629.

[11] V. Jose, H. Hu, E. Edison, W. Manalastas Jr., H. Ren, P. Kidkhunthod, S. Sreejith, A. Jayakumar, J.M.V. Nsanzimana, M. Srinivasan, J. Choi, J.-M. Lee, Modulation of single atomic Co and Fe sites on hollow carbon nanospheres as oxygen electrodes for rechargeable Zn–air batteries, Small Methods 5 (2021), 2000751.

[12] Y. Wang, M. Wu, J. Li, H. Huang, J. Qiao, In situ growth of CoP nanoparticles anchored on (N,P) co-doped porous carbon engineered by MOFs as advanced bifunctional oxygen catalyst for rechargeable Zn–air battery, J. Mater. Chem. A 8 (2020) 19043.

[13] J. Chen, B. Ni, J. Hu, Z. Wu, W. Jin, Defective graphene aerogel-supported Bi–CoP nanoparticles as a high-potential air cathode for rechargeable Zn–air batteries, J. Mater. Chem. A 7 (2019) 22507–22513.

[14] H. Jin, Z. Kou, W. Cai, H. Zhou, P. Ji, B. Liu, A. Radwan, D. He, S. Mu, P–Fe bond oxygen reduction catalysts toward high-efficiency metal–air batteries and fuel cells, J. Mater. Chem. A 8 (2020) 9121–9127.

[15] Y.P. Li, Y. Liu, Q.Z. Qian, G.R. Wang, G.Q. Zhang, Supramolecular assisted one-pot synthesis of donut-shaped CoP@PNC hybrid nanostructures as multifunctional electrocatalysts for rechargeable Zn-air batteries and self-powered hydrogen production, Energy Storage Mater. 28 (2020) 27–36.

[16] H. Liu, J. Guan, S. Yang, Y. Yu, R. Shao, Z. Zhang, M. Dou, F. Wang, Q. Xu, Metal–organic-framework-derived Co_2P nanoparticle/multi-doped porous carbon as a trifunctional electrocatalyst, Adv. Mater. 32 (2020), 2003649.

[17] J. Zhu, Q. He, Y. Liu, J. Key, S. Nie, M. Wu, P.K. Shen, Three-dimensional, hetero-structured, $Cu_3P@C$ nanosheets with excellent cycling stability as Na-ion battery anode material, J. Mater. Chem. A 7 (2019) 16999–17007.

[18] L. Liu, Q. Li, Z. Wang, J. Yan, Y. Chen, Progress of metal-phosphide electrodes for advanced sodium-ion batteries, Funct. Mater. Lett. 11 (2018), 1830001.

[19] Y. Chen, S. Ji, Y. Wang, J. Dong, W. Chen, Z. Li, R. Shen, L. Zheng, Z. Zhuang, D. Wang, Y. Li, Isolated single iron atoms anchored on N-doped porous carbon as an efficient electrocatalyst for the oxygen reduction reaction, Angew. Chem. Int. Ed. 56 (2017) 6937–6941.

[20] X. Zhang, R. Zhao, Q. Wu, W. Li, C. Shen, L. Ni, H. Yan, G. Diao, M. Chen, Petal-like MoS_2 nanosheets space-confined in hollow mesoporous carbon spheres for enhanced lithium storage performance, ACS Nano 11 (2017) 8429–8436.

[21] W. Jin, J. Chen, B. Liu, J. Hu, Z. Wu, W. Cai, G. Fu, Oxygen vacancy–rich in-doped CoO/CoP heterostructure as an effective air cathode for rechargeable Zn–air batteries, Small 15 (2019), 1904210.

[22] S. Chen, L. Zhao, J. Ma, Y. Wang, L. Dai, J. Zhang, Edge-doping modulation of N, P-codoped porous carbon spheres for high-performance rechargeable Zn-air batteries, Nano Energy 60 (2019) 536–544.

[23] X. Ao, W. Zhang, B. Zhao, Y. Ding, G. Nam, L. Soule, A. Abdelhafiz, C. Wang, M. Liu, Atomically dispersed Fe–N–C decorated with Pt-alloy core–shell nanoparticles for improved activity and durability towards oxygen reduction, Energy Environ. Sci. 13 (2020) 3032–3040.

[24] S. Riyajuddin, S.K. Tarik Aziz, S. Kumar, G.D. Nessim, K. Ghosh, 3D-graphene decorated with g-C₃N₄/Cu₃P composite: a noble metal-free bifunctional electrocatalyst for overall water splitting, ChemCatChem 12 (2020) 1394–1402.

[25] F. Yang, X. Liu, H. Zhang, J. Zhou, J. Jiang, X. Lu, Boosting oxygen catalytic kinetics of carbon nanotubes by oxygen-induced electron density modulation for advanced Zn-Air batteries, Energy Storage Mater. 30 (2020) 138–145.

[26] Y. Chang, J. Chen, J. Jia, X. Hu, H. Yang, M. Jia, Z. Wen, The fluorine-doped and defects engineered carbon nanosheets as advanced electrocatalysts for oxygen electroreduction, Appl. Catal. B: Environ. 284 (2021), 119721.

[27] X. Luo, Z. Li, M. Luo, C. Guo, L. Sun, S. Lan, R. Luo, L. Huang, Y. Qin, Z. Luo, Boosting the primary Zn–air battery oxygen reduction performance with mesopore-dominated semi-tubular doped-carbon nanostructures, J. Mater. Chem. A 8 (2020) 9832–9842.

[28] D.C. Nguyen, D.T. Tran, T.L.L. Doan, D.H. Kim, N.H. Kim, J.H. Lee, Rational Design of Core@shell Structured CoSₓ@Cu₂MoS₄Hybridized MoS₂/N,S-Codoped Graphene as Advanced Electrocatalyst for Water Splitting and Zn-Air Battery, Adv. Energy Mater. 10 (2020), 1903289.

[29] Y. Song, X. Xin, S. Guo, Y. Zhang, L. Yang, B. Wang, X. Li, One-step MOFs-assisted synthesis of intimate contact MoP-Cu₃P hybrids for photocatalytic water splitting, Chem. Eng. J. 384 (2020) 123337.

[30] J. Guo, B. Wang, D. Yang, Z. Wan, P. Yan, J. Tian, T.T. Isimjan, X. Yang, Rugae-like Ni₂P-CoP nanoarrays as a bi-functional catalyst for hydrogen generation: NaBH₄ hydrolysis and water reduction, Appl. Catal. B: Environ. 265 (2020) 118584.

[31] Q. Shi, Q. Liu, Y. Ma, Z. Fang, Z. Liang, G. Shao, B. Tang, W.Y. Yang, L. Qin, X. S. Fang, High-performance trifunctional electrocatalysts based on FeCo/Co₂P hybrid nanoparticles for zinc-air battery and self-powered overall water splitting, Adv. Energy Mater. 10 (2020), 1903854.

[32] H. Song, Y. Li, L. Shang, Z. Tang, T. Zhang, S. Lu, Designed controllable nitrogen-doped carbon-dots-loaded MoP nanoparticles for boosting hydrogen evolution reaction in alkaline medium, Nano Energy 72 (2020), 104730.

[33] W. Xiao, L. Zhang, D. Bukhvalov, Z. Chen, Z. Zou, L. Shang, X. Yang, D. Yan, F. Han, T. Zhang, Hierarchical ultrathin carbon encapsulating transition metal doped MoP electrocatalysts for efficient and pH-universal hydrogen evolution reaction, Nano Energy 70 (2020), 104445.

[34] C. Cheng, S. Zong, J. Shi, F. Xue, Y. Zhang, X. Guan, B. Zheng, J. Deng, L. Guo, Facile preparation of nanosized MoP as cocatalyst coupled with g-C₃N₄ by surface bonding state for enhanced photocatalytic hydrogen production, Appl. Catal. B: Environ. 265 (2020) 118620.

[35] J. Li, X. Li, P. Liu, X. Zhu, R.N. Ali, H. Naz, Y. Yu, B. Xiang, Self-supporting hybrid Fiber mats of Cu₃P–Co₂P/N–C endowed with enhanced lithium/sodium ions storage performances, ACS Appl. Mater. Interfaces 11 (2019) 11442–11450.

[36] J. Chen, C. Fan, X. Hu, C. Wang, Z. Huang, G. Fu, J.-M. Lee, Y. Tang, Hierarchically porous Co/CoxMy (M = P, N) as an efficient Mott–Schottky electrocatalyst for oxygen evolution in rechargeable Zn–air batteries, Small 15 (2019), 1901518.

[37] J. Sun, G. Zheng, H.-W. Lee, N. Liu, H. Wang, H. Yao, W. Yang, Y. Cui, Formation of stable phosphorus–carbon bond for enhanced performance in black phosphorus nanoparticle–graphite composite battery anodes, Nano Lett. 14 (2014) 4573–4580.

[38] R. Wang, X.-Y. Dong, J. Du, J.-Y. Zhao, S.-Q. Zang, MOF-derived bifunctional Cu₃P nanoparticles coated by a N,P-codoped carbon shell for hydrogen evolution and oxygen reduction, Adv. Mater. 30 (2017), 1703711.

[39] M. Qian, M. Xu, S. Zhou, J. Tian, T. Taylor Isimjan, Z. Shi, X. Yang, Template synthesis of two-dimensional ternary nickel-cobalt-nitrogen co-doped porous carbon film: promoting the conductivity and more active sites for oxygen reduction, J. Colloid Interface Sci. 564 (2020) 276–285.

[40] X. Feng, Q. Jiao, W. Chen, Y. Dang, Z. Dai, S.L. Suib, J. Zhang, Y. Zhao, H. Li, C. Feng, Cactus-like NiCo₂S₄@NiFe LDH hollow spheres as an effective oxygen

[41] bifunctional electrocatalyst in alkaline solution, Appl. Catal. B: Environ. 286 (2021), 119869.

[41] J. Balamurugan, T.T. Nguyen, N.H. Kim, D.H. Kim, J.H. Lee, Novel core-shell CuMo-oxynitride@N-doped graphene nanohybrid as multifunctional catalysts for rechargeable zinc-air batteries and water splitting, Nano Energy 85 (2021), 105987.

[42] M.F. Sanad, A.R. Puente Santiago, S.A. Tolba, M.A. Ahsan, O. Fernandez-Delgado, M. Shawky Adly, E.M. Hashem, M. Mahrous Abodouh, M.S. El-Shall, S. T. Sreenivasan, N.K. Allam, L. Echegoyen, Co–Cu bimetallic metal organic framework catalyst outperforms the Pt/C benchmark for oxygen reduction, J. Am. Chem. Soc. 143 (2021) 4064–4073.

[43] S.L. Zhang, B.Y. Guan, X.W. Lou, Co–Fe alloy/N-doped carbon hollow spheres derived from dual metal–organic frameworks for enhanced electrocatalytic oxygen reduction, Small 15 (2019), 1805324.

[44] Y. Yuan, J. Wang, S. Adimi, H. Shen, T. Thomas, R. Ma, J.P. Attfield, M. Yang, Zirconium nitride catalysts surpass platinum for oxygen reduction, Nat. Mater. 19 (2020) 282–286.

[45] G. Lv, Y. Wu, Y. Wang, W. Kang, H. Zhang, M. Zhou, Z. Huang, J. Li, Z. Guo, Y. Wang, Rational design of perfect interface coupling to boost electrocatalytical oxygen reduction, Nano Energy 76 (2020), 105055.

[46] T. Zhou, W. Xu, N. Zhang, Z. Du, C. Zhong, W. Yan, H. Ju, W. Chu, H. Jiang, C. Wu, Y. Xie, Ultrathin cobalt oxide layers as electrocatalysts for high-performance flexible Zn–air batteries, Adv. Mater. 31 (2019), 1807468.

[47] L. Chen, L.L. Cui, Z. Wang, X. He, W. Zhang, T. Asefa, Co₈FeS₈/N,S-doped carbons derived from Fe-Co/S-bridged polyphthalocyanine: efficient dual-function air-electrode catalysts for rechargeable Zn-air batteries, ACS Sustain. Chem. Eng. 8 (2020) 13147–13158.

[48] J. Han, X. Meng, L. Lu, J. Bian, Z. Li, C. Sun, Single-atom Fe-Nₓ-C as an efficient electrocatalyst for zinc–air batteries, Adv. Funct. Mater. 29 (2019), 1808872.

[49] R. Zhao, Q. Li, Z. Chen, V. Jose, X. Jiang, G. Fu, J.-M. Lee, S. Huang, B, N-doped ultrathin carbon nanosheet superstructure for high-performance oxygen reduction reaction in rechargeable zinc-air battery, Carbon 164 (2020) 398–406.

[50] Y.-j. Wu, X.-h. Wu, T.-x. Tu, P.-f. Zhang, J.-t. Li, Y. Zhou, L. Huang, S.-g. Sun, Controlled synthesis of FeNₓ-CoNₓ dual active sites interfaced with metallic Co nanoparticles as bifunctional oxygen electrocatalysts for rechargeable Zn-air batteries, Appl. Catal. B: Environ. 278 (2020), 119259.

[51] J. Li, S. Chen, N. Yang, M. Deng, S. Ibraheem, J. Deng, J. Li, L. Li, Z. Wei, Ultrahigh-loading zinc single-atom catalyst for highly efficient oxygen reduction in both acidic and alkaline media, Angew. Chem. Int. Ed. 58 (2019) 7035–7039.

[52] X.B. Zhang, X. Han, Z. Jiang, J. Xu, L.N. Chen, Y.K. Xue, A.M. Nie, Z.X. Xie, Q. Kuang, L.S. Zheng, Atomically dispersed hierarchically ordered porous Fe-N-C electrocatalyst for high performance electrocatalytic oxygen reduction in Zn-Air battery, Nano Energy 71 (2020), 104547.

[53] X. Wang, L. Peng, N. Xu, M. Wu, Y. Wang, J. Guo, S. Sun, J. Qiao, Cu/S-occupation bifunctional oxygen catalysts for advanced rechargeable zinc–air batteries, ACS Appl. Mater. Interfaces 12 (2020) 52836–52844.

[54] R. Boppella, J. Tan, J. Wang, J. Moon, Homologous CoP/NiCoP heterostructure on N-doped carbon for highly efficient and pH-universal hydrogen evolution electrocatalysis, Adv. Funct. Mater. 29 (2018), 1807976.

[55] M. Qiao, Y. Wang, Q. Wang, G. Hu, X. Mamat, S. Zhang, S. Wang, Hierarchically ordered porous carbon with atomically dispersed FeN₄ for ultraefficient oxygen reduction reaction in proton-exchange membrane fuel cells, Angew. Chem. Int. Ed. 59 (2020) 2688–2694.

[56] Q. Zhou, Z. Zhang, J. Cai, B. Liu, Y. Zhang, X. Gong, X. Sui, A. Yu, L. Zhao, Z. Wang, Z. Chen, Template-guided synthesis of Co nanoparticles embedded in hollow nitrogen doped carbon tubes as a highly efficient catalyst for rechargeable Zn-air batteries, Nano Energy 71 (2020) 104592.